galaxies

MDPI

Review

X-ray Polarimetry of X-ray Pulsars

Juri Poutanen *, Sergey S. Tsygankov and Sofia V. Forsblom

Department of Physics and Astronomy, FI-20014 University of Turku, Finland; sergey.tsygankov@utu.fi (S.S.T.); sofia.v.forsblom@utu.fi (S.V.F.)

* Correspondence: juri.poutanen@utu.fi

Abstract: Radiation from X-ray pulsars (XRPs) was expected to be strongly linearly polarized owing to a large difference in their ordinary and extraordinary mode opacities. The launch of *IXPE* allowed us to check this prediction. *IXPE* observed a dozen X-ray pulsars, discovering pulse-phase dependent variation of the polarization degree (PD) and polarization angle (PA). Although the PD showed rather erratic profiles resembling flux pulse dependence, the PA in most cases showed smooth variations consistent with the rotating vector model (RVM), which can be interpreted as a combined effect of vacuum birefringence and dipole magnetic field structure at a polarization-limiting (adiabatic) radius. Application of the RVM allowed us to determine XRP geometry and to confirm the free precession of the NS in Her X-1. Deviations from RVM in two bright transients led to the discovery of an unpulsed polarized emission likely produced by scattering off the accretion disk wind.

Keywords: neutron stars; polarization; pulsars; X-ray binaries

Citation: Poutanen, J.; Tsygankov, S.S.; Forsblom, S.V. X-ray Polarimetry of X-ray Pulsars. *Galaxies* **2024**, *12*, 46. https://doi.org/10.3390/galaxies12040046

Academic Editor: Margo Aller

Received: 30 June 2024
Revised: 23 July 2024
Accepted: 3 August 2024
Published: 7 August 2024

1. Introduction

Classical X-ray pulsars (XRPs) are neutron stars (NSs) found in binary systems, accreting material from companion stars via an accretion disk or stellar wind (for a review, see [1]). The ultra-strong magnetic field of the NSs of the order of $10^{12–13}$ G is able to significantly alter the accretion flow's structure at distances of hundreds of NS radii. At this distance, known as the magnetospheric radius, the magnetic pressure balances the ram pressure in the disk. Consequently, closer to the NS, ionized gas is funneled along magnetic field lines to the magnetic poles, where its kinetic energy is released in the form of X-rays.

The geometrical structure of this emission region and the corresponding beam pattern of an XRP depend strongly on the mass accretion rate. Particularly, it was demonstrated theoretically that there exists a so-called critical luminosity defining two major regimes of accretion [2–4]. Below this threshold, emission originates from the hot spots at the NS's surface, while above it, the radiation pressure is able to stop the infalling matter above the star surface, and an accretion column begins to grow, thus drastically changing the structure of the emitting region. The absolute value of the critical luminosity is a non-monotonic function of the magnetic field strength and has a typical value of 10^{37} erg s^{-1} [4].

The primary observables from XRPs, including energy spectra and light curves, contain information about the geometrical configuration of the emitting regions at the NS surface. However, this information is heavily degenerate with very complex and uncertain physics of emission mechanisms and radiation transfer under the conditions of extremely strong magnetic fields. Therefore, an independent tool sensitive to the geometry is required to address the longstanding challenge of determining the configurations of the emitting regions in XRPs.

Existing theoretical models predicted XRPs to be among the most polarized sources in the X-ray sky. This is due to the birefringence of the medium in a strong magnetic field. Specifically, photon propagation through such a medium can be considered in terms of two normal polarization modes: the so-called ordinary 'O' and extraordinary 'X' photons [5,6]. Due to the different orientations of the photons' electric field vector

oscillation with respect to the plane defined by the directions of the magnetic field and photon momentum, the cross section of interaction between these photons and matter is very different for the two modes. Namely, below the cyclotron frequency, the Compton scattering cross section for the O-mode radiation is much lower than that for the X-mode (see, for example, [7,8]). Many authors have addressed the polarization properties of XRPs [9–15], often predicting a very high polarization degree (PD), reaching nearly 100%. The most recent models cover the low [16,17] and the high [18] mass accretion rates with a thin slab and accretion column geometries, respectively, also predicting a substantial PD in excess of 30% in the standard X-ray range 2–10 keV. A relatively low polarization degree (PD) remains possible at low mass accretion rates due to the inverse temperature profile in the atmosphere of an accreting NS [16,19]. The verification of different model predictions requires sensitive polarimetric observations.

In addition to the emission produced at the magnetic poles, one expects contributions to the polarized emission also from the reflection of that radiation off the NS surface, accretion disk, accretion disk wind, accretion curtain, stellar wind, and stellar surface (see Figure 1). Some of these components are expected to be pulsating with the pulsar frequency, some may be pulse-phase independent, and some may depend on the orbital phase. Separating the contribution of these components is a difficult task, and X-ray polarimetry may provide an avenue for the solution.

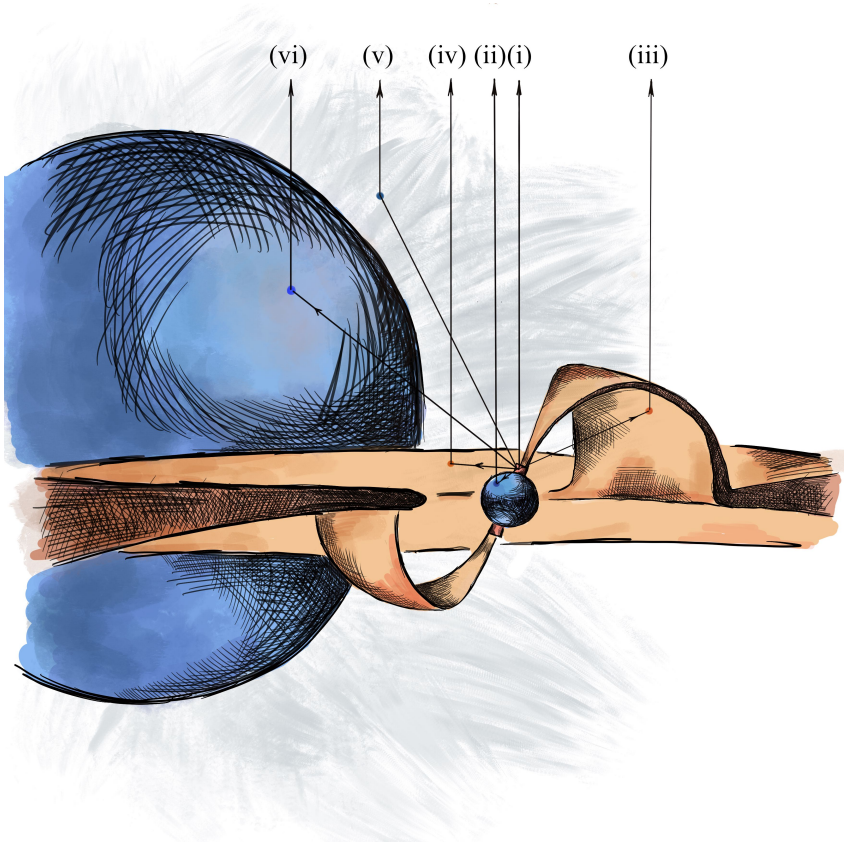

Figure 1. Possible sources of polarized emission in XRPs: (i) intrinsic polarization from the hotspot, (ii) reflection from the NS surface, (iii) reflection from the accretion curtain, (iv) reflection from the accretion disk (and accretion disk wind), (v) scattering off the stellar wind, and (vi) reflection off the optical companion. From [20].

A handful of attempts have been made to detect the polarization of XRPs. Already in 1975, OSO-8 observed Cen X-3 and Her X-1 to search for X-ray polarization [21] with no significant polarization detected either in pulse phase-averaged or phase-resolved data. The balloon-borne hard X-ray polarimeter X-Calibur operating in the 15–35 keV energy

range observed GX 301−2, resulting in no significant detection of polarization [22]. The successful launch in December 2021 of the *Imaging X-ray polarimetry Explorer* (*IXPE*; [23]), which has a sensitivity of at least two orders of magnitude higher than OSO-8 [24], allowed us to obtain significant detection of polarization in a dozen XRPs and to test theoretical models. Here, we review the results of the *IXPE* observations of XRPs during the first two years of operations in orbit.

2. Rotating Vector Model

The rotating vector model (RVM) was introduced in the 1960s [25,26] to describe the polarization from radio pulsars. In this model, the evolution of the PA with pulsar phase is related to the projection of the magnetic dipole on the plane of the sky. The same model was suggested by Meszaros et al. [15] to be used for modeling the X-ray polarization of XRPs. The main reason why the RVM should work for strongly magnetized NSs is that because of vacuum birefringence [6,27], photon polarization direction is adjusted to the local magnetic field geometry until the adiabatic radius is reached (e.g., [28–30]). This radius is estimated to be ∼20 NS radii for photons in the *IXPE* range and the typical surface magnetic field strength detected in XRPs [31,32]:

$$R_{\rm ad} \sim 2 \times 10^7 \left(\frac{E}{4\,{\rm keV}}\right)^{1/5} \left(\frac{B}{10^{12}\,{\rm G}}\right)^{2/5} \left(\frac{R_{\rm NS}}{12\,{\rm km}}\right)^{6/5} {\rm cm}. \quad (1)$$

At such distances, the field is expected to be dominated by the dipole component. We expect, therefore, to measure polarization either parallel or perpendicular to the instantaneous projection of the magnetic dipole onto the plane of the sky depending on the intrinsic polarization mode. The phase variation of the PA is thus a purely geometrical effect and does not depend on the behavior of the PD or flux.

If radiation is dominated by the O-mode with the oscillation direction in the plane of the magnetic field and photon momentum, the PA χ measured from the projection of the spin axis on the sky in the counterclockwise direction is given by [33]:

$$\tan(\chi - \chi_{\rm p}) = \frac{-\sin\theta_{\rm p}\,\sin\phi}{\sin i_{\rm p}\cos\theta_{\rm p} - \cos i_{\rm p}\sin\theta_{\rm p}\cos\phi}, \quad (2)$$

where $\chi_{\rm p}$ is the position angle (measured from north to east) of the pulsar angular momentum, $i_{\rm p}$ is the inclination of the pulsar spin with respect to the line of sight, and $\theta_{\rm p}$ is the magnetic obliquity, i.e., the angle between the magnetic dipole and the spin axis (see Figure 2 for geometry).

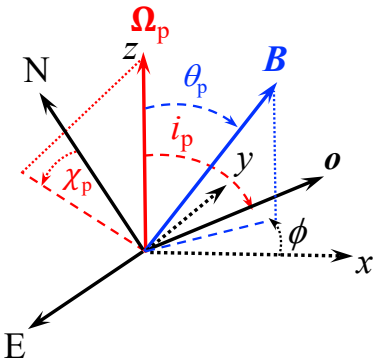

Figure 2. Geometry of the pulsar and main parameters of the RVM. The pulsar angular momentum $\boldsymbol{\Omega}_{\rm p}$ makes an angle $i_{\rm p}$ with respect to the observer direction $\boldsymbol{o}$. The angle $\theta_{\rm p}$ is the magnetic obliquity, i.e., the angle between magnetic dipole $\boldsymbol{B}$ and the rotation axis. Pulsar phase ϕ is the azimuthal angle of vector $\boldsymbol{B}$ in the plane (x, y) perpendicular to $\boldsymbol{\Omega}_{\rm p}$ measured from the projection of $\boldsymbol{o}$. The pulsar position angle $\chi_{\rm p}$ is the angle measured counterclockwise between the direction to the north (N) and the projection of $\boldsymbol{\Omega}_{\rm p}$ on the plane of the sky (N-E).

For radiation in the X-mode, the PA χ is rotated by 90° with respect to the O-mode. We note that in slow XRPs, the general relativistic effects such as light bending do not affect the expression for the PA because photon trajectories are planar in the Schwarzschild metric. For NSs rotating at millisecond periods, the special relativity effects need to be accounted for, and also the general relativistic effects become important [33,34].

Let us now consider a simple toy model for XRP polarization. We consider emission from two point-like antipodal hotspots at the NS surface. We assume the intensity and the PD of radiation escaping from the hotspot to vary with the zenith angle α as

$$I(\alpha) = I_0\,(1 + a\cos\alpha), \quad P = P_{\max}(1-\cos\alpha)/(1+b\cos\alpha). \tag{3}$$

Positive a corresponds to the pencil-like emission pattern, while the negative a to the fan-like pattern. The expression for the PD implies that polarization is zero along the normal to the surface, $\alpha = 0$, because of the axial symmetry and monotonically growing with the zenith angle. The angle between the magnetic dipole (normal to the primary spot) and the direction to the observer ψ varies with the pulsar phase ϕ as:

$$\cos\psi_{\rm p} = \cos i_{\rm p}\cos\theta_{\rm p} + \sin i_{\rm p}\sin\theta_{\rm p}\cos\phi. \tag{4}$$

For the secondary spot in the southern hemisphere, $\cos\psi_{\rm s} = -\cos\psi_{\rm p}$. For a slowly rotating NS, we can use the Schwarzschild metric to describe gravitational light bending. For calculations, we use an accurate analytical expression for the relation $\alpha(\psi)$ given by Equation (2) in [35]. The observed flux is then $F \propto \mathcal{D}\; I(\alpha)\cos\alpha$, with the lensing factor $\mathcal{D} \propto d\cos\alpha/d\cos\psi$ given by Equation (17) in [35]. The visibility condition for every spot reads $\cos\alpha > 0$. The Stokes parameters for each spot are given by the products $Q_i = F_i\,P_i\,\cos 2\chi$ and $U_i = F_i\,P_i\,\sin 2\chi$. Summing up the Stokes vectors for two spots $F = F_1 + F_2$, $Q = Q_1 + Q_2$, and $U = U_1 + U_2$, we obtain the total Stokes vector describing the linearly polarized light observed from the XRP. The normalized Stokes parameters can be defined as $q = Q/F$ and $u = U/F$. To demonstrate what kind of polarization is expected in this model and to develop physical intuition, we compute three cases reflecting different geometries. The pulse phase dependencies of the normalized flux, the PD, and PA together with the trajectories and XRP left on the (q,u) plane are shown in Figure 3.

The first thing to notice is the apparent anticorrelation between the flux and PD, which is a result of assuming a pencil-beam emission with $a > 0$. For $a < 0$, one expects a correlation. In the first case (black solid lines), $(i_{\rm p},\theta_{\rm p})$=(60°, 30°), the observer is looking at the magnetic dipole from a side, and both hotspots are visible all the time. The PA shows an S-shape profile. We note that the clockwise rotation of the pulsar (i.e., replacing $i_{\rm p} \to 180^\circ - i_{\rm p}$) produces PA of an opposite sign (and shifted by half a period), and therefore can be easily distinguished from the counterclockwise rotation. The (q,u) trajectory is a 'kidney'-like shape outside of the origin, with the exact shape, of course, depending on the angular distributions of $I(\alpha)$ and PD(α). In the second case (red dotted lines), $(i_{\rm p},\theta_{\rm p})$=(30°, 70°), the observer sees the position angle of the dipole making a 360° rotation during the period, which is reflected in the sawtooth behavior of the phase dependence of the PA with a nearly constant derivative dPA/dϕ. For the counterclockwise rotation of the XRP $i_{\rm p} < 90^\circ$, the PA grows with the phase, while for $i_{\rm p} > 90^\circ$, the PA decreases. The source leaves a pretzel-like trace in the (q,u) plane with two loops going around the origin. The third considered case (blue dashed lines), $(i_{\rm p},\theta_{\rm p})$=(70°, 85°), corresponds to a nearly orthogonal rotator with the observer at a high inclination. We see 2-peak pulses corresponding to the two hotspots coming close to the line of sight with a strong variations in the PD reaching maxima at minima fluxes at phases 0.25 and 0.75. The PA still shows a sawtooth appearance but with a strongly varying derivative dPA/dϕ. The trajectory at the (q,u) plane has a rather complicated moth-like shape with two close approaches to the origin at phases 0 and 0.5. A non-zero pulsar spin position angle $\chi_{\rm p}$ results in a corresponding shift of the PA and rotation of the trajectories in the (q,u) plane by the angle $2\chi_{\rm p}$.

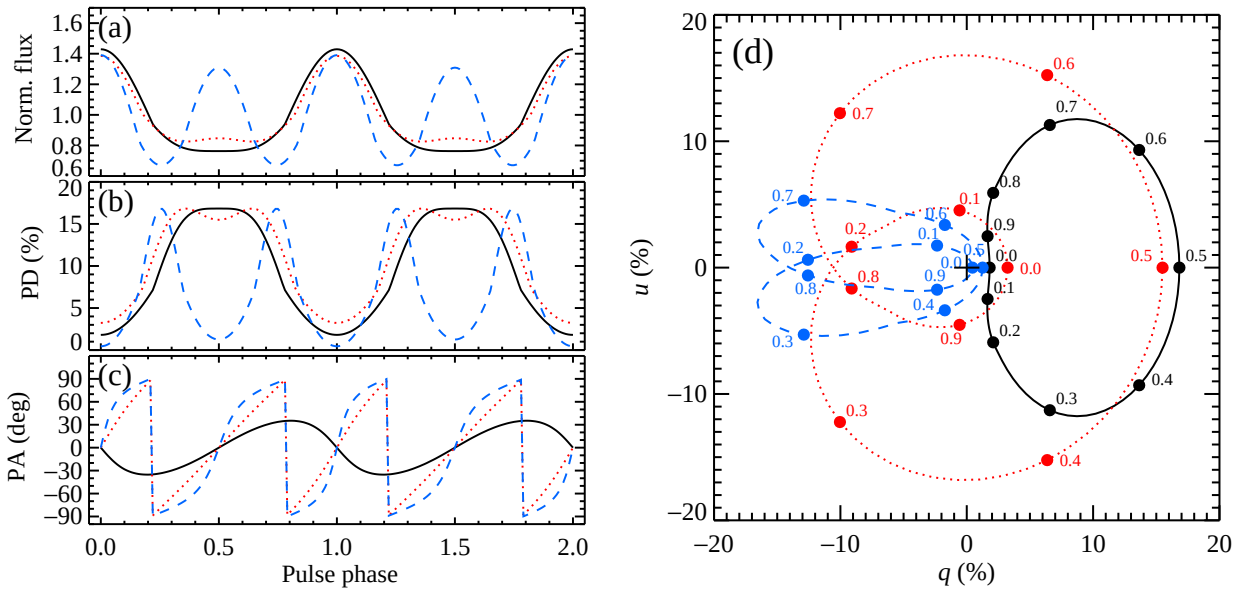

Figure 3. Examples of the RVM with the emission pattern and polarization given by Equation (3). (**a**) Normalized flux, (**b**) PD, and (**c**) PA as functions of pulse phase for various pairs of parameters (i_p, θ_p). The case of $(60°, 30°)$ is shown with black solid lines, $(30°, 70°)$ with red dotted lines, and $(70°, 85°)$ with blue dashed lines. (**d**) Evolution of normalized Stokes parameters (q, u) for the same three sets of pairs. The numbers mark the pulse phase. We use here the following parameters: the NS mass $M = 1.4 M_\odot$ and radius of 12 km, $a = 1$, $b = 0.5$, $P_{max} = 30\%$, and $\chi_p = 0$.

3. X-ray Pulsars Observed by *IXPE*

During the first two years of operations in orbit, *IXPE* observed eleven XRPs, with several of them a few times in different states (see Table 1). The results are presented in a series of papers [20,36–47]. As discussed previously, the high PD from magnetized NS is expected due to the large difference in cross sections between the two polarization modes at energies below the cyclotron resonance. As can be seen from the table, the working energy range of *IXPE* (2–8 keV) is significantly below the cyclotron energy for all XRPs in our sample, fulfilling the conditions for a high PD.

Table 1. Parameters of XRPs observed by *IXPE*.

Name	Spin Period [a,b] [s]	Orbital Period [a,b] [d]	Distance [a,b] [kpc]	Luminosity [c] [erg s^{-1}]	CRSF [d] [keV]	*IXPE* Reference
Cen X-3	4.8	2.09	6.07	1.9×10^{37}	28	[36]
Her X-1	1.24	1.7	7.09	$\sim 3 \times 10^{37}$	37	[37,38]
4U 1626-67	7.7	0.02875	15.08	6.4×10^{36}	37, 61?	[39]
Vela X-1	283	8.96	1.87	3.8×10^{35}	25, 53	[40]
GRO J1008-57	93.5	249.5	3.21	$(0.6–1.6) \times 10^{36}$	78	[41]
EXO 2030+375	41.31	46.02	2.08	1.3×10^{36}	36/63?	[42]
X Persei	837.67	250.3	0.63	1.2×10^{34}	29	[20]
GX 301-2	696.0	41.59	3.54	1.3×10^{36}	37/50	[43]
LS V +44 17	202.5	155.0	2.29	$\leq 4 \times 10^{37}$	32	[44]
Swift J0243.6+6124	9.87	28.3	5.2	$(0.6–2.4) \times 10^{37}$	146	[45]
SMC X-1	0.717	3.892	61	2×10^{38}	–	[46]

[a] XRBcats: Galactic High Mass X-ray Binary Catalog [48]. [b] XRBcats: Galactic low-mass X-ray binary catalog [49]. [c] X-ray luminosity during *IXPE* observations. [d] Energy of the cyclotron resonance spectral feature from [50]. Question mark identifies uncertain detections.

Observations of XRPs with *IXPE* started with the first two sources of this class discovered at the dawn of X-ray astronomy, Cen X-3 and Her X-1. Both sources have a nearly

critical luminosity of around 10^{37} erg s^{-1}. First and the most striking discovery made for both sources is a rather low PD, much below all theoretical predictions. Particularly, for Cen X-3, the PD was found to be only $5.8 \pm 0.3\%$ in the phase-averaged data [36]. Here, it is worth mentioning that due to the rotation of the NS, one might expect a reduction in the PD in the phase-averaged signal. Therefore, for all *IXPE* papers on XRPs, a lot of attention was given to the accurate timing solution required for the proper phase-resolved polarimetric analysis.

After splitting all photons from Cen X-3 into 12 bins over the spin cycle of the NS, significant variations in both PD and PA over the pulse phase were discovered. In particular, it was found that PD shows a significant anticorrelation with the pulsed flux (inline with the predictions by [15] for a sub-critical XRP), reaching a maximum value of around 15%, which is still much lower than the theoretical predictions (see left panels in Figure 4). The authors discuss several mechanisms potentially responsible for the low value of PD (see below). The PA value was also found to vary over the pulse phase (Figure 4, left). As discussed in Section 2, such variation can be used to derive the geometrical parameters of the NSs in XRPs. For Cen X-3, the pulsar spin position angle and the magnetic obliquity were estimated to be about 49° and 17°, respectively (see Table 2 for RVM parameters).

Table 2. RVM parameters of the XRPs observed by *IXPE*.

Name	$i_{\rm p}$ [deg]	$\theta_{\rm p}$ [deg]	$\chi_{\rm p}$ [deg]
Cen X-3	70.2 (fixed)	16.4 ± 1.3	49.2 ± 1.1
Her X-1 (main-on)	56^{+24}_{-20}	$3.7^{+2.6}_{-1.9}$	42 ± 2
Her X-1 (short-on)	90 ± 30	$16.3^{+3.5}_{-4.1}$	57.9 ± 2.1
GRO J1008−57	130 ± 3	74 ± 2	75 ± 4
EXO 2030+375	128^{+8}_{-6}	60^{+5}_{-6}	-30^{+4}_{-5}
X Persei	162 ± 12	90 ± 15	70 ± 30
GX 301−2	135 ± 17	43 ± 12	135
LS V +44 17/Obs. 1	56 ± 12	27 ± 4	82 ± 1
LS V +44 17/Obs. 2	102 ± 2	54 ± 1	-6.2 ± 0.4
LS V +44 17 [a]	108 ± 2	48 ± 1	-8.4 ± 0.6
Swift J0243/Obs. 1	80 ± 3	87 ± 2	-70 ± 4
Swift J0243/Obs. 2	60 ± 5	88 ± 3	-87 ± 7
Swift J0243/Obs. 3	33 ± 7	75 ± 5	-66 ± 7
Swift J0243 [a]	25^{+8}_{-17}	77^{+2}_{-29}	-44^{+12}_{-13}
SMC X-1	91^{+41}_{-42}	13^{+7}_{-6}	87 ± 4

[a] Obtained using two-component model to the combined data set.

Another famous XRP, Her X-1, was observed several times during the first two years of *IXPE*. The reason for that is a 35 d super-orbital periodicity presumably related to free or/and forced precession of the NS in this unique system (see [51] and references therein). In total, *IXPE* performed five observations of the source, three times in the so-called "main-on" state and two times during the "short-on" state. The first two observations were utilized to determine the geometrical parameters of the NS using the RVM. Moreover, combining X-ray and optical polarimetric data, it was found that the spin axis of the NS and the angular momentum of the binary orbit are misaligned by about 20° [37]. In addition to that, a marginally significant variability of PA over the super-orbital cycle was revealed (Table 2). This effect was later confirmed with additional observations of the source (see Figure 5) [38,47]. The detailed modeling of the pulse phase-resolved data at different super-orbital phases allowed [38] to conclude that the observed 35 d period in Her X-1 is set by the free precession of the NS crust, implying that its shape is slightly asymmetric, by a few parts per ten million. In addition to that, the authors found indications that the NS geometry is altered by torques on a time scale of a few hundred days.

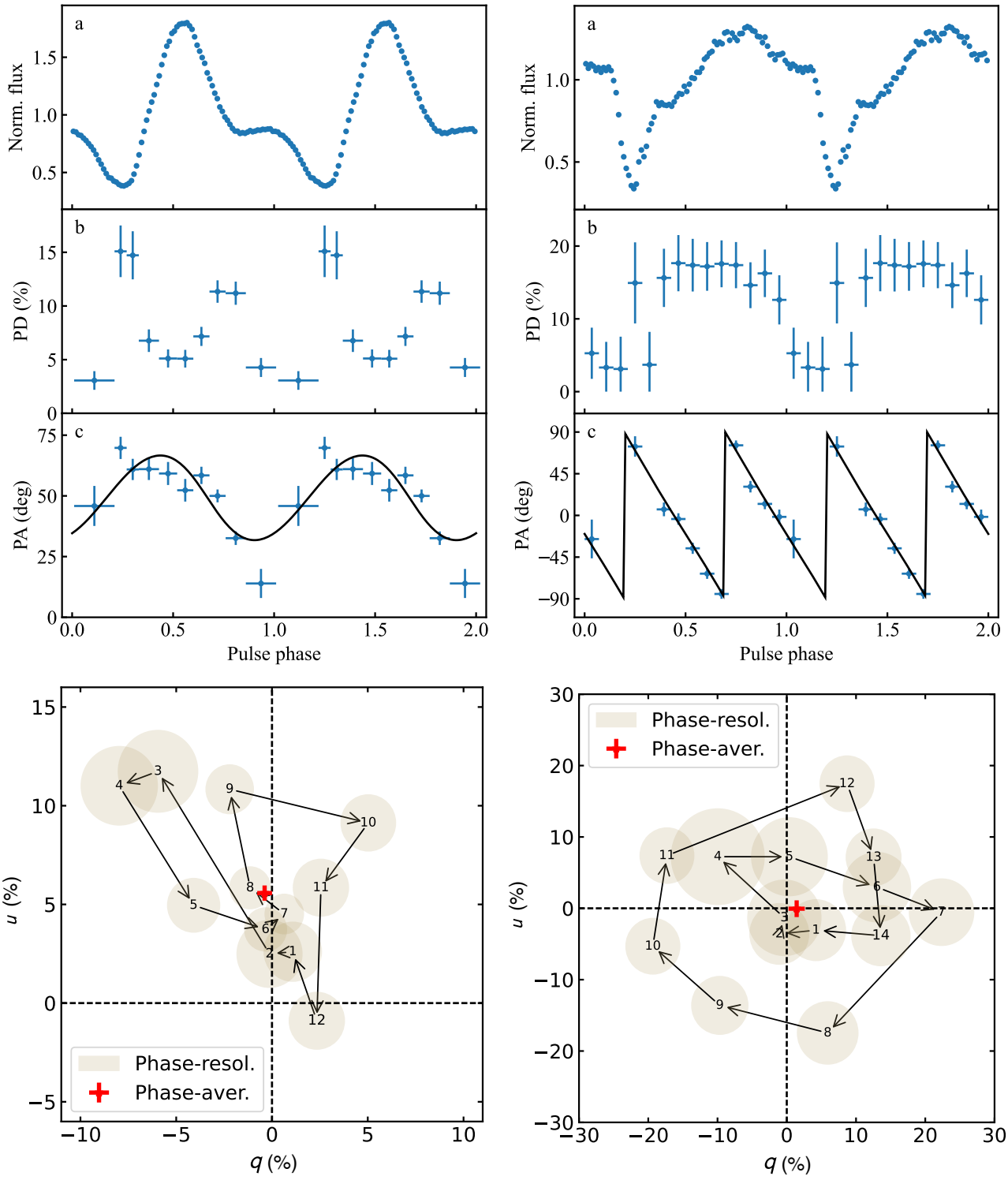

Figure 4. Examples of the phase-resolved spectropolarimetric analysis for two XRPs: Cen X-3 (**left**) and X Persei (**right**). The evolutions of the normalized flux (pulse profile), PD, and PA are shown in the corresponding panels (**a**–**c**). The lower panels demonstrate the phase-resolved behavior of the normalized Stokes parameters q and u.

Thanks to the energy resolution capabilities of *IXPE*, it is possible to study the energy dependence of the polarization properties of XRPs, albeit in a rather narrow range of 2–8 keV. The majority of sources from our sample do not show any significant dependence of PD or PA on energy. However, for X Persei, a very strong increase in the PD from ∼0%

at 2 keV to ∼30% at 8 keV was discovered [20]. The reason for such behavior is still under debate. Applying the RVM to the phase-resolved polarimetric data allowed the authors to demonstrate that the magnetic obliquity in this source is very close to 90°, making X Persei a so-called orthogonal rotator (see right panels of Figure 4 and compare to the red dotted line in Figure 3d). Moreover, the direct correlation of the PD and flux over the pulse phase observed in this source contrasts with the pattern observed in Cen X-3 (compare left and right panels in Figure 4) and the predictions [15]. A possible reason for such behavior is an inverse temperature profile in the NS atmosphere at low mass accretion rates (see below) and, correspondingly, the modified beam pattern [20].

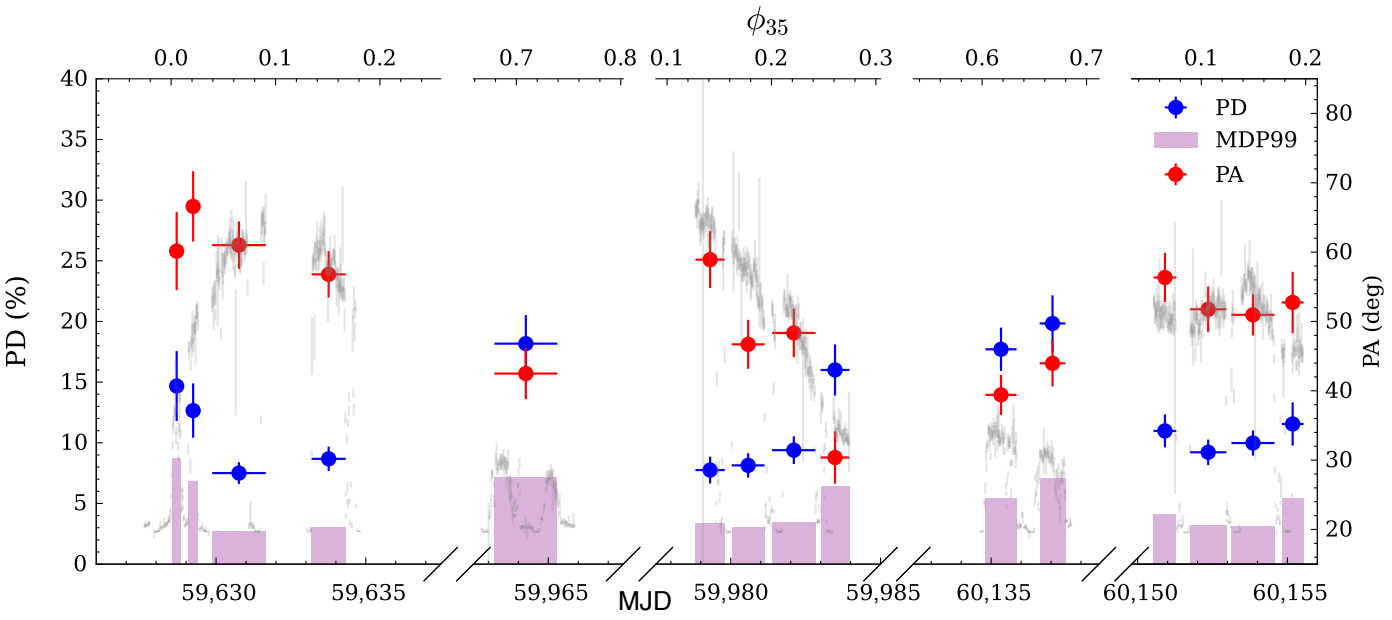

Figure 5. Evolution of the pulse-phase average PD (blue circles, left axis) and the PA (red circles, right axis) of Her X-1 with time (lower axis) and the super-orbital phase (upper axis). The pink rectangles show the minimum detectable polarization at 99% CL. The gray symbols show the flux evolution. From [47].

In the case of Vela X-1, the energy dependence of the polarimetric properties looks even more interesting. First, at low energies, the PD value decreases with energy, reaching a minimum around ∼3.5 keV [40]. Above this energy, it starts to increase, reaching around 10% at 8 keV. However, the most fascinating fact is that the PA makes a 90° swing between low and high energies. This, combined with a very complex pulse profile shape, results in very complicated phase-resolved variations of the PA, which cannot be fit with the RVM. Therefore, Vela X-1 remains an XRP with still unknown geometry.

Several sources were observed several times as a function of their luminosity. One such XRP is GRO J1008−57, observed by *IXPE* two times during the outburst in November 2022 [41]. The luminosities of the source during both observations differed by only a factor of ∼2, resulting in almost identical polarimetric properties, which allowed authors to increase counting statistics by combining two data sets. Phase-resolved spectro-polarimetric analysis of the combined data revealed a picture very similar to that of X Persei: positive correlation of the PD with the pulsed flux and large magnetic obliquity (∼75°).

The only extragalactic XRP, SMC X-1, was observed with *IXPE* also several times covering a significant fraction of its ∼45 d super-orbital cycle [46]. Another distinctive feature of this pulsar is a very high observed luminosity ($L_{2-8\,\mathrm{keV}} \approx 2 \times 10^{38}\,\mathrm{erg\,s^{-1}}$), making SMC X-1 the most luminous XRP ever observed by *IXPE*. In spite of the clearly super-critical regime of accretion, the polarization properties of the source are very similar to the ones observed from much weaker XRPs Cen X-3: low peak PD value around 10%

and anticorrelation of the PD with the flux over the pulse phase. Applying the RVM to three consecutive observations allowed the authors to reveal a gradual drift of the position angle of the pulsar, possibly indicating scattering in the wind of the precessing accretion disk observed at a large inclination.

In addition to the XRPs discussed above, *IXPE* observed several objects where the counting statistics did not allow for a detailed analysis. Specifically, in GX 301-2 [43] and EXO 2030+375 [42], polarization was significantly detected only in a few phase bins. However, this did not preclude the authors from determining the geometrical parameters in these systems using the RVM (see Table 2).

Although in all XRPs discussed above, the observed PD was low, it was detected significantly in at least the phase-resolved data. The only exception is 4U 1626-67, the only XRP from the *IXPE* sample in an ultracompact low-mass X-ray binary, in which even phase-resolved analysis did not result in significant measurement of the PD [39]. Only marginal evidence of a non-zero polarization of the power-law component at the $4.8 \pm 2.3\%$ level was found in the combined phase-resolved spectro-polarimetric modeling.

As was mentioned above, one of the most striking results obtained by *IXPE* for XRPs is a very low PD, significantly below the theoretical predictions. Different authors discussed multiple reasons for that. In particular, [37] suggested a physical reason related to the thermal structure of the NS atmosphere valid for XRPs accreting at sub-critical rates when the energy of the infalling matter is dissipated at the NS surface, heating its upper atmosphere. In the case of a nearly critical mass accretion rate, the emergent radiation escapes primarily perpendicular to the normal direction to the NS surface, forming a "fan"-like beam pattern. A simplified calculation by [37] indicates the possibility to obtain a low PD value if the vacuum resonance, where the contributions of plasma and magnetized vacuum to the dielectric tensor cancel each other and mixing of the normal modes of radiation occurs, is located in the transition atmospheric layer with a sharp temperature gradient. Geometrical factors such as the combined emission observed simultaneously from two poles at different angles also might be a reason for the low PD values in XRPs with luminosities in a wide range. In the case of very bright XRPs ($\gtrsim 10^{38}$ erg s^{-1}), a substantial fraction of emission from the NS is intercepted by the optically thick envelop and scattered, leading to the depolarization effect [45,46].

Most of the XRP polarimetric data can be well described by the RVM. However, sometimes the RVM parameters change with time. Their variation in Her X-1 can be explained by precession [38,47]. Sometimes, the variations are just too large for us to believe in the changes of the geometry. The first case of that sort was the bright transient XRP RX J0440.9+4431/LS V +44 17 that went to the outburst in the beginning of 2023. *IXPE* performed two observations separated by two weeks. The pulse profile showed some variations (Figure 6a), and the PD grew from less than 10% to more than 15% (Figure 6b) when the flux dropped just by 30%. To our big surprise, the PA varied dramatically (see Figure 6c). Although the RVM fits the PA phase dependence rather well, the parameters varied wildly (see Table 2 and [44]), with, for example, the pulsar inclination and magnetic obliquity changed by $\sim 40^\circ$ and $\sim 30^\circ$, respectively, and $\chi_{\rm p}$ rotated by $\sim 90^\circ$. Although the latter change might be related to a switch between the modes, strong variations in the other parameters in just two weeks was difficult to understand.

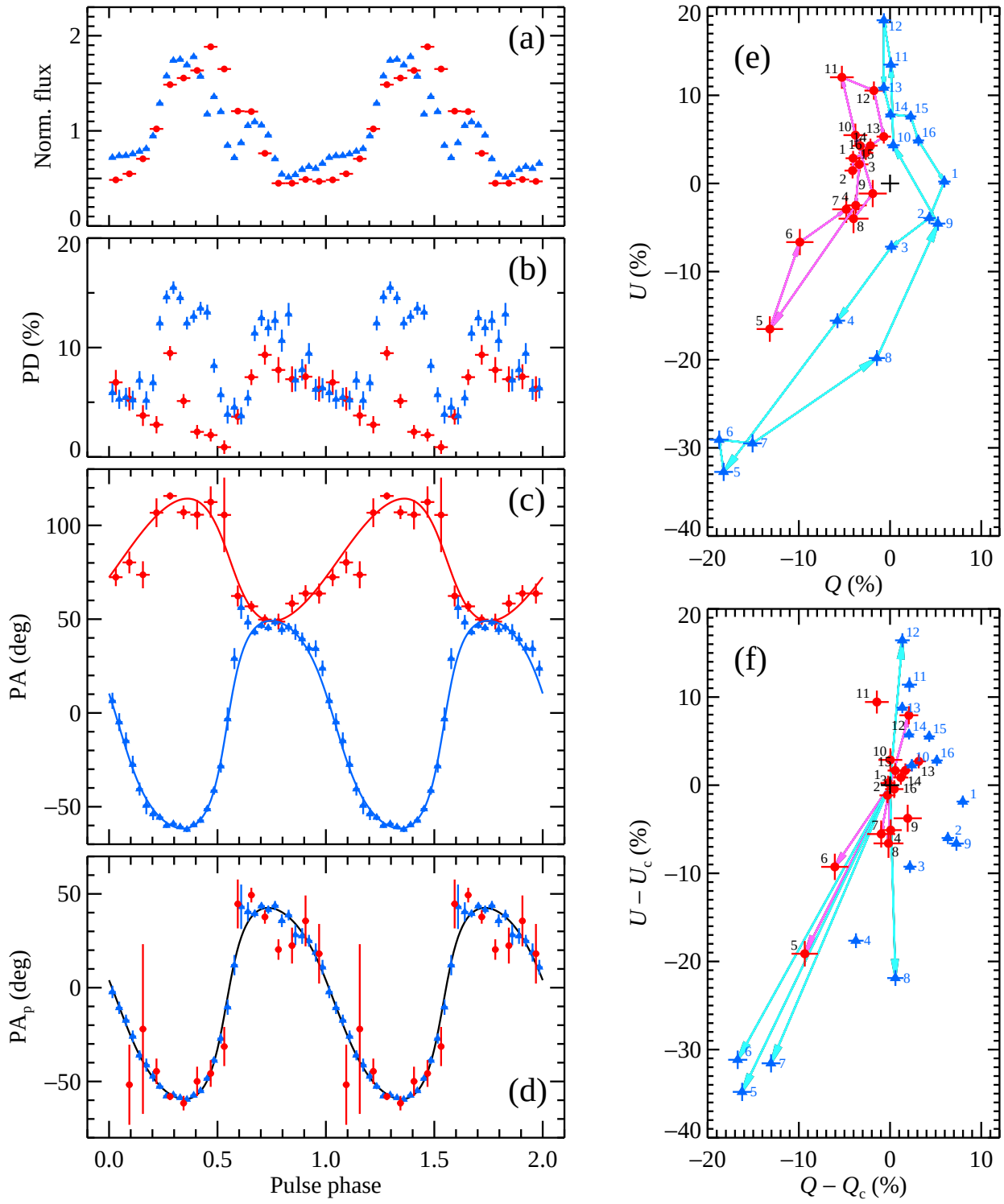

Figure 6. Pulse phase dependence of polarimetric characteristics of XRP LS V +44 17. (**a**) Normalized flux, (**b**) PD, (**c**) PA, and (**d**) intrinsic PA after subtraction of the constant component. Red circles and blue triangles correspond to two observations separated by two weeks. Adapted from [44]. Panel (**e**) shows the observed phase-resolved *absolute* Stokes parameters Q and U (scaled to the mean flux) rebinned to the same phase intervals. The numbers mark the bins from 1 to 16, and the arrows connect the data points. The black cross is the origin. Panel (**f**) is the same diagram with the constant component subtracted. The arrows now connect the origin to a few selected points, illustrating that the arrows corresponding to the same phase bin in the two observations are nearly parallel, implying similar PA.

A detailed look at the tracks that the source leaves on the Stokes parameter plane reveals that they are very similar (see Figure 6e), but the amplitude is larger in the second observation, and, what is even more important, the tracks lie on the different sides of the origin, resulting in very different PAs. This fact brought us to the idea that there are two polarized components in the LS V +44 17 data. The first one is associated with the pulsar and is described by the RVM. The second one is independent of the pulsar phase. In this case, the *absolute* (but possibly scaled, e.g., to the average flux value) Stokes parameters for each observation can be expressed as a sum of the variable and constant components:

$$\begin{aligned} I(\phi) &= I_{\rm c} + I_{\rm p}(\phi), \\ Q(\phi) &= Q_{\rm c} + P_{\rm p}(\phi) I_{\rm p}(\phi) \cos[2\chi(\phi)], \\ U(\phi) &= U_{\rm c} + P_{\rm p}(\phi) I_{\rm p}(\phi) \sin[2\chi(\phi)]. \end{aligned} \tag{5}$$

Here, indices denote the constant (c) and pulsed (p) components. The Stokes parameters of the constant component are additional fit parameters. The RVM now has to fit the PA of the variable component for both observations that can be obtained from

$$\chi(\phi) = \frac{1}{2} \arctan\left[\frac{U(\phi) - U_{\rm c}}{Q(\phi) - Q_{\rm c}}\right]. \tag{6}$$

To illustrate this two-component model, we plot the intrinsic Stokes parameters, i.e., those where the best-fit constant component is subtracted, in Figure 6f. If, before the subtraction, the PA for the two observations at the same phases had completely different values (Figure 6c), then after the subtraction, the PAs are similar as illustrated by the green arrows in Figure 6f, and can be fitted with the common RVM (see Figure 6d).

From the best-fit Stokes parameters of the constant component $Q_{\rm c}$ and $U_{\rm c}$, one can obtain the polarized flux of that component $P_{\rm c} I_{\rm c} = \sqrt{Q_{\rm c}^2 + U_{\rm c}^2}$ which turned out to be 3–4.5% (of the pulse-average flux) depending on the observation. Interestingly, the PA of the constant component $\chi_{\rm c}$ was found to be consistent with the PA of the optical emission $\chi_{\rm o}$ in LS V +44 17. These two facts were interpreted as evidence in favor of the accretion disk being responsible for the constant polarized component and the accretion disk and the Be-star decretion disk being coplanar. Radiation scattered in an equatorial outflow is polarized parallel to the disk axis with the dependence on inclination PD = $\sin^2 i/(3 - \cos^2 i)$ [52] and thus can reach a value of 33% for edge-on observers. Furthermore, the PD drops slowly with decreasing inclination and depends rather weakly on the vertical extent of the wind. Alternatively, the pulsar radiation can be scattered off the accretion curtain, where the disk interacts with the magnetosphere. The values of a few percent for $P_{\rm c} I_{\rm c}$ can be achieved if, for example, the constant component is polarized at a level of $\sim$20% and it contributes $\sim$10–20% to the total flux; these numbers are realistic in the accretion wind scenario. On the other hand, the position angle of the pulsar spin $\chi_{\rm p}$ was found to be different by $\sim 75^\circ$ (or $\sim 15^\circ$ if pulsar radiation is dominated by the X-mode) from $\chi_{\rm c}$, implying a possible misalignment between the pulsar spin and the orbital axes.

In the summer of 2023, ultra-luminous X-ray pulsar Swift J0243.6+6124 went to the outburst, and *IXPE* observed it three times for two days every time with about two-week intervals [45]. This XRP also showed variations in polarimetric properties but not as extreme as LS V +44 17. On two occasions, the PA showed a sine-wave like pattern but with half a period and during the last observations, and the PA showed a clear sawtooth pattern implying $i_{\rm p} < \theta_{\rm p}$. Because the first two data sets cannot be modeled with pure RVM, the two-component model was applied, leading to a much better description of the data and allowing to obtain the geometrical parameters (Table 2). In this object, the polarized flux of the constant component $P_{\rm c} I_{\rm c}$ varied between 1.5% and 3%, and a $\sim 60^\circ$ difference was found between $\chi_{\rm c}$ and $\chi_{\rm p}$, implying a misalignment angle between the pulsar spin and the orbital axes exceeding 30°. On the other hand, in this object, the optical PA $\chi_{\rm o}$ and $\chi_{\rm c}$ were barely consistent with each other, indicating a possible misalignment between the accretion and decretion disk axes.

4. Summary

All existing theoretical models of emission from accreting XRPs predict very high PD, up to 80%, making them the most promising targets for X-ray polarimeters. The launch of the *IXPE* observatory provided the first opportunity to verify these predictions and thus probe our understanding of radiation transport in the presence of extremely strong magnetic fields.

The first two years of *IXPE* operations have demonstrated a complete inconsistency between our expectations and reality. Specifically, in none of the observed XRPs (around a dozen in total) did the PD exceed 15–20%, with typical values varying between 5 and 15%. In one source, low-mass X-ray binary 4U 1626-67, the polarization was not detected, with upper limits around 5%. In all other XRPs, both PD and PA showed significant variability over the pulse phase.

In contrast to the PD, which sometimes resembles a complex pulse profile shape, the PA demonstrates very smooth and simple variations over the pulse phase. This is related to quantum-electrodynamics effects and the simple dipole configuration of the NS magnetic field at relatively large distances. This feature allows us to apply the RVM to independently determine the geometrical configuration of XRPs, thereby breaking the longstanding degeneracy between the geometry of the pulsar and the physics of its emission. Thanks to this, it was possible to confirm the free precession of the NS in Her X-1 and discover unpulsed but strongly polarized emissions from the bright transients LS V +44 17 and Swift J0243.6+6124.

The growing sample of NSs with known geometry will play an important role in studies of NS spin evolution in the context of binary systems and will allow tighter constraints on the detection of continuous gravitational waves [53,54]. Future observations of XRPs with *IXPE* will hopefully increase the statistics, allowing us to study the energy dependence of polarimetric characteristics and to shed light on the physical nature of various spectral components. We also hope to catch an outburst of a bright transient XRP to study changes in the polarization between super- and sub-critical regimes of accretion, to learn about the dependence of the emission region structure on the mass accretion rate, and to verify the whole paradigm of accretion onto the highly magnetized NSs.

Author Contributions: Conceptualization and writing the review and editing, J.P. and S.S.T.; data curation, S.V.F. All authors have read and agreed to the published version of the manuscript.

Funding: This research was supported by the Academy of Finland grants 333112 and 349144.

Data Availability Statement: *IXPE* data are available at the HEASARC https://heasarc.gsfc.nasa.gov/docs/archive.html.

Acknowledgments: The authors are grateful to the members of the *IXPE* topical working group on Accreting Neutron Stars and especially Victor Doroshenko and Jeremy Heyl for their important contribution to the analysis and interpretation of the *IXPE* data on X-ray pulsars.

Conflicts of Interest: The authors declare no conflicts of interest.

Abbreviations

The following abbreviations are used in this manuscript:

IXPE	Imaging X-ray Polarimetry Explorer
XRP	X-ray pulsar
NS	Neutron star
PD	Polarization degree
PA	Polarization angle
RVM	Rotating vector model
CRSF	Cyclotron resonance spectral feature

References

1. Mushtukov, A.; Tsygankov, S. Accreting strongly magnetised neutron stars: X-ray Pulsars. In *Handbook of X-ray and Gamma-ray Astrophysics*; Bambi, C., Santangelo, A., Eds.; Springer: Singapore, 2024; pp. 4105–4176. [CrossRef]
2. Basko, M.M.; Sunyaev, R.A. The limiting luminosity of accreting neutron stars with magnetic fields. *Mon. Not. R. Astron. Soc.* **1976**, *175*, 395–417. [CrossRef]
3. Becker, P.A.; Klochkov, D.; Schönherr, G.; Nishimura, O.; Ferrigno, C.; Caballero, I.; Kretschmar, P.; Wolff, M.T.; Wilms, J.; Staubert, R. Spectral formation in accreting X-ray pulsars: Bimodal variation of the cyclotron energy with luminosity. *Astron. Astrophys.* **2012**, *544*, A123. [CrossRef]
4. Mushtukov, A.A.; Suleimanov, V.F.; Tsygankov, S.S.; Poutanen, J. The critical accretion luminosity for magnetized neutron stars. *Mon. Not. R. Astron. Soc.* **2015**, *447*, 1847–1856. [CrossRef]
5. Gnedin, Y.N.; Pavlov, G.G. The transfer equations for normal waves and radiation polarization in an anisotropic medium. *Sov. J. Exp. Theor. Phys.* **1974**, *38*, 903–908.
6. Gnedin, Y.N.; Pavlov, G.G.; Shibanov, Y.A. The effect of vacuum birefringence in a magnetic field on the polarization and beaming of X-ray pulsars. *Sov. Astron. Lett.* **1978**, *4*, 117–119.
7. Harding, A.K.; Lai, D. Physics of strongly magnetized neutron stars. *Rep. Prog. Phys.* **2006**, *69*, 2631–2708. [CrossRef]
8. Mushtukov, A.A.; Nagirner, D.I.; Poutanen, J. Compton scattering S matrix and cross section in strong magnetic field. *Phys. Rev. D* **2016**, *93*, 105003. [CrossRef]
9. Nagel, W. Radiative transfer in a strongly magnetized plasma. I—Effects of anisotropy. II—Effects of Comptonization. *Astrophys. J.* **1981**, *251*, 278–296. [CrossRef]
10. Nagel, W. Radiative Transfer in a Strongly Magnetized Plasma—Part Two—Effects of Comptonization. *Astrophys. J.* **1981**, *251*, 288–296. [CrossRef]
11. Kaminker, A.D.; Pavlov, G.G.; Shibanov, I.A. Radiation from a Strongly Magnetized Plasma—The Case of Predominant Scattering. *Astrophys. Space Sci.* **1982**, *86*, 249–297. [CrossRef]
12. Meszaros, P.; Nagel, W. X-ray pulsar models. I. Angle-dependent cyclotron line formation and comptonization. *Astrophys. J.* **1985**, *298*, 147–160. [CrossRef]
13. Meszaros, P.; Nagel, W. X-ray pulsar models. II. Comptonized spectra and pulse shapes. *Astrophys. J.* **1985**, *299*, 138–153. [CrossRef]
14. Kii, T. X-ray polarization from accreting strongly magnetized neutron stars :case studies for the X-ray pulsars 4U 1626−67 and Hercules X-1. *Publ. Astron. Soc. Jpn.* **1987**, *39*, 781–800.
15. Meszaros, P.; Novick, R.; Szentgyorgyi, A.; Chanan, G.A.; Weisskopf, M.C. Astrophysical Implications and Observational Prospects of X-ray Polarimetry. *Astrophys. J.* **1988**, *324*, 1056–1067. [CrossRef]
16. Mushtukov, A.A.; Suleimanov, V.F.; Tsygankov, S.S.; Portegies Zwart, S. Spectrum formation in X-ray pulsars at very low mass accretion rate: Monte Carlo approach. *Mon. Not. R. Astron. Soc.* **2021**, *503*, 5193–5203. [CrossRef]
17. Sokolova-Lapa, E.; Gornostaev, M.; Wilms, J.; Ballhausen, R.; Falkner, S.; Postnov, K.; Thalhammer, P.; Fürst, F.; García, J.A.; Shakura, N.; et al. X-ray emission from magnetized neutron star atmospheres at low mass-accretion rates. I. Phase-averaged spectrum. *Astron. Astrophys.* **2021**, *651*, A12. [CrossRef]
18. Caiazzo, I.; Heyl, J. Polarization of accreting X-ray pulsars. I. A new model. *Mon. Not. R. Astron. Soc.* **2021**, *501*, 109–128. [CrossRef]
19. González-Caniulef, D.; Zane, S.; Turolla, R.; Wu, K. Atmosphere of strongly magnetized neutron stars heated by particle bombardment. *Mon. Not. R. Astron. Soc.* **2019**, *483*, 599–613. [CrossRef]
20. Mushtukov, A.A.; Tsygankov, S.S.; Poutanen, J.; Doroshenko, V.; Salganik, A.; Costa, E.; Di Marco, A.; Heyl, J.; La Monaca, F.; Lutovinov, A.A.; et al. X-ray polarimetry of X-ray pulsar X Persei: Another orthogonal rotator? *Mon. Not. R. Astron. Soc.* **2023**, *524*, 2004–2014. [CrossRef]
21. Silver, E.H.; Weisskopf, M.C.; Kestenbaum, H.L.; Long, K.S.; Novick, R.; Wolff, R.S. The first search for X-ray polarization in the Centaurus X-3 and Hercules X-1 pulsars. *Astrophys. J.* **1979**, *232*, 248–254. [CrossRef]
22. Abarr, Q.; Baring, M.; Beheshtipour, B.; Beilicke, M.; de Geronimo, G.; Dowkontt, P.; Errando, M.; Guarino, V.; Iyer, N.; Kislat, F.; et al. Observations of a GX 301-2 Apastron Flare with the X-Calibur Hard X-ray Polarimeter Supported by NICER, the Swift XRT and BAT, and Fermi GBM. *Astrophys. J.* **2020**, *891*, 70. [CrossRef]
23. Weisskopf, M.C.; Soffitta, P.; Baldini, L.; Ramsey, B.D.; O'Dell, S.L.; Romani, R.W.; Matt, G.; Deininger, W.D.; Baumgartner, W.H.; Bellazzini, R.; et al. The Imaging X-ray Polarimetry Explorer (IXPE): Pre-Launch. *J. Astron. Telesc. Instrum. Syst.* **2022**, *8*, 026002. [CrossRef]
24. Soffitta, P.; Baldini, L.; Bellazzini, R.; Costa, E.; Latronico, L.; Muleri, F.; Del Monte, E.; Fabiani, S.; Minuti, M.; Pinchera, M.; et al. The Instrument of the Imaging X-ray Polarimetry Explorer. *Astron. J.* **2021**, *162*, 208. [CrossRef]
25. Radhakrishnan, V.; Cooke, D.J. Magnetic Poles and the Polarization Structure of Pulsar Radiation. *Astrophys. Lett.* **1969**, *3*, 225.
26. Komesaroff, M.M. Possible Mechanism for the Pulsar Radio Emission. *Nature* **1970**, *225*, 612–614. [CrossRef]
27. Pavlov, G.G.; Shibanov, Y.A. Influence of vacuum polarization by a magnetic field on the propagation of electromagnetic waves in a plasma. *Sov. J. Exp. Theor. Phys.* **1979**, *49*, 741.
28. Heyl, J.S.; Shaviv, N.J. Polarization evolution in strong magnetic fields. *Mon. Not. R. Astron. Soc.* **2000**, *311*, 555–564. [CrossRef]

29. Heyl, J.S.; Shaviv, N.J. QED and the high polarization of the thermal radiation from neutron stars. *Phys. Rev. D* **2002**, *66*, 023002. [CrossRef]
30. Taverna, R.; Turolla, R.; Gonzalez Caniulef, D.; Zane, S.; Muleri, F.; Soffitta, P. Polarization of neutron star surface emission: A systematic analysis. *Mon. Not. R. Astron. Soc.* **2015**, *454*, 3254–3266. [CrossRef]
31. Heyl, J.; Caiazzo, I. Strongly Magnetized Sources: QED and X-ray Polarization. *Galaxies* **2018**, *6*, 76. [CrossRef]
32. Taverna, R.; Turolla, R. X-ray Polarization from Magnetar Sources. *Galaxies* **2024**, *12*, 6. [CrossRef]
33. Poutanen, J. Relativistic rotating vector model for X-ray millisecond pulsars. *Astron. Astrophys.* **2020**, *641*, A166. [CrossRef]
34. Loktev, V.; Salmi, T.; Nättilä, J.; Poutanen, J. Oblate Schwarzschild approximation for polarized radiation from rapidly rotating neutron stars. *Astron. Astrophys.* **2020**, *643*, A84. [CrossRef]
35. Poutanen, J. Accurate analytic formula for light bending in Schwarzschild metric. *Astron. Astrophys.* **2020**, *640*, A24. [CrossRef]
36. Tsygankov, S.S.; Doroshenko, V.; Poutanen, J.; Heyl, J.; Mushtukov, A.A.; Caiazzo, I.; Di Marco, A.; Forsblom, S.V.; González-Caniulef, D.; Klawin, M.; et al. The X-ray Polarimetry View of the Accreting Pulsar Cen X-3. *Astrophys. J. Lett.* **2022**, *941*, L14. [CrossRef]
37. Doroshenko, V.; Poutanen, J.; Tsygankov, S.S.; Suleimanov, V.F.; Bachetti, M.; Caiazzo, I.; Costa, E.; Di Marco, A.; Heyl, J.; La Monaca, F.; et al. Determination of X-ray pulsar geometry with IXPE polarimetry. *Nat. Astron.* **2022**, *6*, 1433–1443. [CrossRef]
38. Heyl, J.; Doroshenko, V.; González-Caniulef, D.; Caiazzo, I.; Poutanen, J.; Mushtukov, A.; Tsygankov, S.S.; Kirmizibayrak, D.; Bachetti, M.; Pavlov, G.G.; et al. Complex rotational dynamics of the neutron star in Hercules X-1 revealed by X-ray polarization. *Nat. Astron.* 2024, *in press*. [CrossRef]
39. Marshall, H.L.; Ng, M.; Rogantini, D.; Heyl, J.; Tsygankov, S.S.; Poutanen, J.; Costa, E.; Zane, S.; Malacaria, C.; Agudo, I.; et al. Observations of 4U 1626-67 with the Imaging X-ray Polarimetry Explorer. *Astrophys. J.* **2022**, *940*, 70. [CrossRef]
40. Forsblom, S.V.; Poutanen, J.; Tsygankov, S.S.; Bachetti, M.; Di Marco, A.; Doroshenko, V.; Heyl, J.; La Monaca, F.; Malacaria, C.; Marshall, H.L.; et al. IXPE Observations of the Quintessential Wind-accreting X-ray Pulsar Vela X-1. *Astrophys. J. Lett.* **2023**, *947*, L20. [CrossRef]
41. Tsygankov, S.S.; Doroshenko, V.; Mushtukov, A.A.; Poutanen, J.; Di Marco, A.; Heyl, J.; La Monaca, F.; Forsblom, S.; Malacaria, C.; Marshall, H.L.; et al. X-ray pulsar GRO J1008-57 as an orthogonal rotator. *Astron. Astrophys.* **2023**, A48. [CrossRef]
42. Malacaria, C.; Heyl, J.; Doroshenko, V.; Tsygankov, S.S.; Poutanen, J.; Forsblom, S.V.; Capitanio, F.; Di Marco, A.; Du, Y.; Ducci, L.; et al. A polarimetric-oriented X-ray stare at the accreting pulsar EXO 2030+375. *Astron. Astrophys.* **2023**, *675*, A29. [CrossRef]
43. Suleimanov, V.F.; Forsblom, S.V.; Tsygankov, S.S.; Poutanen, J.; Doroshenko, V.; Doroshenko, R.; Capitanio, F.; Di Marco, A.; González-Caniulef, D.; Heyl, J.; et al. X-ray polarimetry of the accreting pulsar GX 301-2. *Astron. Astrophys.* **2023**, *678*, A119. [CrossRef]
44. Doroshenko, V.; Poutanen, J.; Heyl, J.; Tsygankov, S.S.; Caiazzo, I.; Turolla, R.; Veledina, A.; Weisskopf, M.C.; Forsblom, S.V.; González-Caniulef, D.; et al. Complex variations in X-ray polarization in the X-ray pulsar LS V +44 17/RX J0440.9+4431. *Astron. Astrophys.* **2023**, *677*, A57. [CrossRef]
45. Poutanen, J.; Tsygankov, S.S.; Doroshenko, V.; Forsblom, S.V.; Jenke, P.; Kaaret, P.; Berdyugin, A.V.; Blinov, D.; Kravtsov, V.; Liodakis, I.; et al. Studying geometry of the ultraluminous X-ray pulsar Swift J0243.6+6124 using X-ray and optical polarimetry. *arXiv* **2024**, arXiv:2405.08107. [CrossRef]
46. Forsblom, S.V.; Tsygankov, S.S.; Poutanen, J.; Doroshenko, V.; Mushtukov, A.A.; Ng, M.; Ravi, S.; Marshall, H.L.; Di Marco, A.; La Monaca, F.; et al. Probing the polarized emission from SMC X-1: The brightest X-ray pulsar observed by IXPE. *arXiv* **2024**, arXiv:2406.08988. [CrossRef]
47. Zhao, Q.C.; Li, H.C.; Tao, L.; Feng, H.; Zhang, S.N.; Walter, R.; Ge, M.Y.; Tong, H.; Ji, L.; Zhang, L.; et al. Polarization perspectives on Hercules X-1: Further constraining the geometry. *Mon. Not. R. Astron. Soc.* **2024**, *531*, 3935–3949. [CrossRef]
48. Neumann, M.; Avakyan, A.; Doroshenko, V.; Santangelo, A. XRBcats: Galactic High Mass X-ray Binary Catalogue. *Astron. Astrophys.* **2023**, *677*, A134. [CrossRef]
49. Avakyan, A.; Neumann, M.; Zainab, A.; Doroshenko, V.; Wilms, J.; Santangelo, A. XRBcats: Galactic low-mass X-ray binary catalogue. *Astron. Astrophys.* **2023**, *675*, A199. [CrossRef]
50. Staubert, R.; Trümper, J.; Kendziorra, E.; Klochkov, D.; Postnov, K.; Kretschmar, P.; Pottschmidt, K.; Haberl, F.; Rothschild, R.E.; Santangelo, A.; et al. Cyclotron lines in highly magnetized neutron stars. *Astron. Astrophys.* **2019**, *622*, A61. [CrossRef]
51. Kolesnikov, D.; Shakura, N.; Postnov, K. Evidence for neutron star triaxial free precession in Her X-1 from Fermi/GBM pulse period measurements. *Mon. Not. R. Astron. Soc.* **2022**, *513*, 3359–3367. [CrossRef]
52. Sunyaev, R.A.; Titarchuk, L.G. Comptonization of low-frequency radiation in accretion disks Angular distribution and polarization of hard radiation. *Astron. Astrophys.* **1985**, *143*, 374–388. [CrossRef]
53. Piccinni, O.J. Status and Perspectives of Continuous Gravitational Wave Searches. *Galaxies* **2022**, *10*, 72. [CrossRef]
54. Wette, K. Searches for continuous gravitational waves from neutron stars: A twenty-year retrospective. *Astropart. Phys.* **2023**, *153*, 102880. [CrossRef]